
The Neural Pruning Law Hypothesis

Eugen Barbulescu
eugen.barbulescu@aut.utcluj.ro

Antonio Alexoai
antonio.alexoai@aut.utcluj.ro

Lucian Busoni
lucian.busoni@aut.utcluj.ro

Abstract

Network pruning is used to reduce inference latency and power consumption in large neural networks. However, most current pruning methods rely on ad-hoc heuristics that are poorly understood. We introduce Hyperflux, a conceptually-grounded pruning method, and use it to study the pruning process. Hyperflux models this process as an interaction between weight *flux*, the gradient’s response to the weight’s removal, and network *pressure*, a global regularization driving weights towards pruning. We postulate properties that arise naturally from our framework and find that the relationship between minimum flux among weights and density follows a power-law equation. Furthermore, we hypothesize the power-law relationship to hold for any effective saliency metric and call this idea the *Neural Pruning Law Hypothesis*. We validate our hypothesis on several families of pruning methods (magnitude, gradients, L_0), providing a potentially unifying property for neural pruning.

1 Introduction

Overparameterization has become the norm in modern deep learning to achieve state-of-the-art performance (Neyshabur et al., 2019; Allen-Zhu et al., 2019; Li et al., 2018). Despite clear benefits for training, this practice also increases computational and memory costs, complicating deployment on resource-constrained devices such as edge hardware, IoT platforms, and autonomous robots (Shi et al., 2016; Li et al., 2019). Recent theoretical and empirical findings suggest that sparse subnetworks extracted from large dense models can match or exceed the accuracy of their dense counterparts (Frankle and Carbin, 2019; Zhou et al., 2019; Ma et al., 2021; Lee et al., 2019; De Jorge et al., 2021; Cho et al., 2023; Yite et al., 2023; Frantar et al., 2024; Wang et al., 2023) and even outperform smaller dense models of

equal size (Ramanujan et al., 2020; Li et al., 2020; Zhu and Gupta, 2018). These results have created interest in network pruning as a strategy to identify minimal, high-performing subnetworks.

Pruning has a rich history (LeCun et al., 1989; Mozer and Smolensky, 1988; Thimm and Hoppe, 1995) and continues to prove valuable for real-time applications (Han et al., 2016; Jongsoo et al., 2017; Wang et al., 2019). Recent methods have significantly advanced the field by resorting to a variety of strategies, from magnitude pruning, gradient methods, and Hessian-based criteria (Han et al., 2015, 2016; LeCun et al., 1992; Singh and Alistarh, 2020; Bellec et al., 2018; Frankle and Carbin, 2019) to dynamic pruning approaches (Liu et al., 2020; Cho et al., 2023; Savarese et al., 2020; Kusupati et al., 2020; Wortsman et al., 2019) or combinations thereof (Liu et al., 2022; Evci et al., 2020). However, the strong interdependence between weights remains a challenge (Jin et al., 2020; Templeton et al., 2024; Lee et al., 2019; De Jorge et al., 2021; Louizos et al., 2017), as it complicates the task of determining each weight’s importance. Optimal pruning has been explored (Hoefler et al., 2021; LeCun et al., 1992), but such formulations are typically computationally intractable in practice. Overall, the field consists of a variety of seemingly unconnected pruning methods, each trying to approximate importance in its own way.

Given this gap, we ask: *Are there unifying properties for pruning methods?*

To study these properties, we start by creating our own method, based on first principles rather than empirical results and heuristics. Inspired by the principle that *the value of something is not truly known until it is lost*, which has shaped major discoveries in fields such as functional genomics (Giaever et al., 2002; Shalem et al., 2014), neuroscience (Rorden and Karnath, 2004), and network science (Albert et al., 2000), we introduce Hyperflux, an L_0 pruning method that determines a weight’s importance by first removing it and observing the gradient caused as a result, its *flux*.

The main idea of Hyperflux is that each weight has a flux, which appears when the weight is pruned through

the network’s gradients. A global L_0 regularization term called *pressure* pushes all weights towards pruning, aiming to uncover each of their fluxes. Those weights whose flux is greater than the pressure will be regrown, while the rest will remain pruned. This process is repeated until the end of training.

We postulate and empirically confirm two properties that emerge from our framework: density convergence and a relationship between minimum flux among weights and density, for which we find a power-law equation in our experiments. Based on these results, we hypothesize this power-law for any saliency, including those in most pruning methods.

To confirm our hypothesis, we choose 3 established types of pruning methods, magnitude, gradient, L_0 , and verify that the same power-law relationship appears for ResNet-50 and VGG-19 networks on Cifar-10, Cifar-100 and ImageNet datasets respectively. While this is not our main objective, we also observe Hyperflux to be better or competitive to current state-of-the-art methods.

Summarizing, our key contributions are:

- We introduce *Hyperflux*, a conceptually grounded pruning method that obtains competitive results compared to state-of-the-art.
- We study Hyperflux’s mechanisms and build an analytical framework around it, leading us to a power-law relationship between minimum flux among weights and density.
- We hypothesize the power-law relationship between minimum saliency among weights and density to hold across most pruning methods, and verify its existence on 3 families of such methods.

2 Related work

Research on neural network pruning has a relatively old history, with some methods going back decades and laying the groundwork for modern approaches. Early approaches, such as LeCun et al. (1989) and LeCun et al. (1992), utilized Hessian-based techniques and Taylor expansions to identify and remove unimportant specific weights, while Mozer and Smolensky (1988) employed derivatives to remove whole units, an early form of structured pruning. These initial studies demonstrated the feasibility of reducing network complexity without significantly compromising performance. An influential overview Thimm and Hoppe (1995) concluded that magnitude pruning was particularly effective, a paradigm that since then has been widely adopted Han et al. (2016); Frankle and Carbin

(2019); Zhou et al. (2019); Evci et al. (2020); Kusupati et al. (2020); Han et al. (2015); Tai et al. (2022); Peste et al. (2021); Georgoulakis et al. (2023).

The existence of highly effective subnetworks builds upon these foundational studies, with the Lottery Ticket Hypothesis Frankle and Carbin (2019) being a good example. This work uses magnitude pruning to demonstrate that there exists a mask which, if applied at the start of training, produces a sparse subnetwork capable of matching the performance of the original dense network after training, if the initialization is kept unmodified. Subsequent research has further validated this concept by showing that these subnetworks produced by masks, even without any training, achieve significantly higher accuracy than random chance Zhou et al. (2019), reaching up to 80% accuracy on MNIST. Moreover, training these masks instead of the actual weight values can result in performance comparable to the original network Ramanujan et al. (2020); Zhou et al. (2019), suggesting that neural network training can occur through mechanisms different from weight updates, including the masking of randomly initialized weights. Other studies have attempted to identify the most trainable subnetworks at initialization. SNIP Lee et al. (2019) use gradient magnitudes as a way to identify trainable weights, while Savarese et al. (2020) employ L_0 regularization along with a sigmoid function that gradually transitions into a step function during training, enabling continuous sparsification. These findings indicate that the specific values and even the existence of certain weights may be less critical than previously believed.

Dynamic pruning differs from classical heuristics by allowing the model to make pruning decisions while processing the input, without a fixed pattern. Some methods use learnable parameters, e.g. Kusupati et al. (2020) train magnitude thresholds for each layer in the network to determine which weights will be pruned. Other works, like that of Cho et al. (2023), do not have any learnable parameters, learning instead a weight distribution whose shape will determine which and how many weights are pruned. Yet another class of L_0 regularization techniques Savarese et al. (2020); Louizos et al. (2018) try to maximize the number of removed weights. Hyperflux aligns with the dynamic pruning paradigm by enabling continuous pruning of weights based on learnable parameters. However, unlike such methods, Hyperflux does not treat the regularization as a fixed value, but as an adjustable input of the training procedure, which can be used to control its behavior.

Pruning based on gradient values is another prominent approach, often overlapping with dynamic methods, which assesses weight properties in relation to the loss function. Works Lee et al. (2019) and De Jorge

et al. (2021) assess the trainability of subnetworks by analyzing initial gradient magnitudes relative to the loss function. AutoPrune Xiao et al. (2019) introduces handcrafted gradients that influence training, while Dynamic Pruning with Feedback Lin et al. (2020) uses gradients during backpropagation to recover pruned weights with high trainability, preserving accuracy. RigL Evci et al. (2020) use gradient and weight magnitudes to determine which weights to prune and to regrow. GraNet Liu et al. (2022) employs a neuroregeneration scheme, which prunes and regrows the same number of weights, effectively keeping the sparsity constant while growing accuracy. Hyperflux distinguishes itself from all these methods by evaluating the importance of weights *after* the moment of their pruning. Instead of deciding which weights are (un)important based solely on instantaneous gradients or single-stage evaluations, Hyperflux identifies a weight’s significance based on the aggregated impact across topologies its removal has on the network’s performance.

3 Hyperflux method

We associate each weight ω_i to a learnable parameter t_i , which determines whether the weight is present ($t_i > 0$) or pruned ($t_i \leq 0$). We define a weight’s importance to be the increase in loss caused by its pruning. We assess the importance of a weight ω_i through its flux, the gradient of t_i with respect to the loss function when $t_i \leq 0$. The connection between flux and weight importance is detailed in Section 3.2. The *pressure* term, denoted by $L_{-\infty}$, will push all t values towards $-\infty$, pruning the weights and revealing their fluxes. No manual selection or analysis of gradients is needed, since the interaction between pressure and flux during backpropagation will naturally only keep important weights whose flux is large.

3.1 Preliminaries

Consider a neural network defined as a function $f : \mathcal{X} \times \mathbb{R}^d \rightarrow \mathcal{Y}$ where \mathcal{X} is the input space, \mathcal{Y} is the output space, and \mathbb{R}^d is the space of weights. Given a training set $\{(x_j, y_j)\}_{j=1}^J$, learning the weights ω amounts to minimizing a loss function so that $f(x_j, \omega)$ aligns with y_j :

$$\mathcal{L}(\omega) = \sum_{j=1}^J \ell(f(x_j, \omega), y_j),$$

We define the topology of the neural network as a binary vector $\mathcal{T} \in \{0, 1\}^d$ where \mathcal{T}_i represents whether weight ω_i is pruned or not. We denote a family of topologies as $\mathcal{T}^{1 \rightarrow K}$, with K its cardinality and \mathcal{T}^k a specific topology from the family. Thus, the loss of a

network with topology \mathcal{T} is:

$$\mathcal{L}(\omega, \mathcal{T}) = \sum_{j=1}^J \ell(f(x_j, \omega \odot \mathcal{T}), y_j),$$

where \odot is the Hadamard product. For each weight ω_i , we introduce a learnable presence parameter t_i with $t \in \mathbb{R}^d$ denoting the vector collecting all t_i . The vector t is used to generate the topology \mathcal{T} with $\mathcal{T}_i = H(t_i)$, where:

$$H(t_i) = \begin{cases} 1 & \text{if } t_i > 0, \\ 0 & \text{if } t_i \leq 0. \end{cases}$$

Thus, if $t_i > 0$ then ω_i is active, otherwise (when $t_i \leq 0$), ω_i is pruned. We use a global penalty term $L_{-\infty}$ to push all t_i values towards $-\infty$, which we discuss in detail in Section 3.2. Our goal is to find a topology \mathcal{T}^* and set of weights ω^* such that the following loss is minimized:

$$\mathcal{J}(\omega, \mathcal{T}) = \mathcal{L}(\omega, \mathcal{T}) + L_{-\infty}(t).$$

3.2 Flux and pressure

We begin by introducing the notion of flux, evaluated on one topology \mathcal{T} , and develop its connection to weight importance. Since the optimal topology \mathcal{T}^* is initially unknown, any metric measured on some topology \mathcal{T} might not be relevant for \mathcal{T}^* . For this reason, we then extend flux to *aggregated flux*, a more informative evaluation based on a family of topologies $\mathcal{T}^{1 \rightarrow K}$.

We start by defining $\mathcal{G}_i(\omega, \mathcal{T})$, representing the direction in which t_i needs to change to minimize the loss for topology \mathcal{T} and weights ω :

$$\mathcal{G}_i(\omega, \mathcal{T}) = -\frac{\partial \mathcal{L}(\omega, \mathcal{T})}{\partial t_i}, \forall t_i \in \mathbb{R}. \quad (1)$$

To allow computing (1) despite the non-differentiable step function $H(t_i)$, we employ a straight-through estimator for the gradient of H with respect to t_i , which we denote by STE_H . Several choices for STE_H will create the behavior we desire in \mathcal{G} (e.g., $\text{STE}_H(t_i) = \sigma(t_i) \cdot (1 - \sigma(t_i))$, $\text{STE}_H(t_i) = 1 - \tanh^2(t_i)$), but none perform significantly better than the others in experiments. Therefore, for the sake of simplicity, we choose $\text{STE}_H(t_i) = 1$.

To fully understand the implications of \mathcal{G}_i on updating t_i , we study the gradients composing it. We define $\theta_i = \omega_i \cdot H(t_i)$, and refer to θ_i as effective weight. By rewriting \mathcal{G}_i we get:

$$\mathcal{G}_i(\omega, \mathcal{T}) = -\underbrace{\frac{\partial \mathcal{L}(\omega, \mathcal{T})}{\partial \theta_i}}_{=: \mathcal{A}_i} \cdot \frac{\partial \theta_i}{\partial t_i} = \mathcal{A}_i \cdot \omega_i \cdot \text{STE}_H(t_i) = \mathcal{A}_i \cdot \omega_i.$$

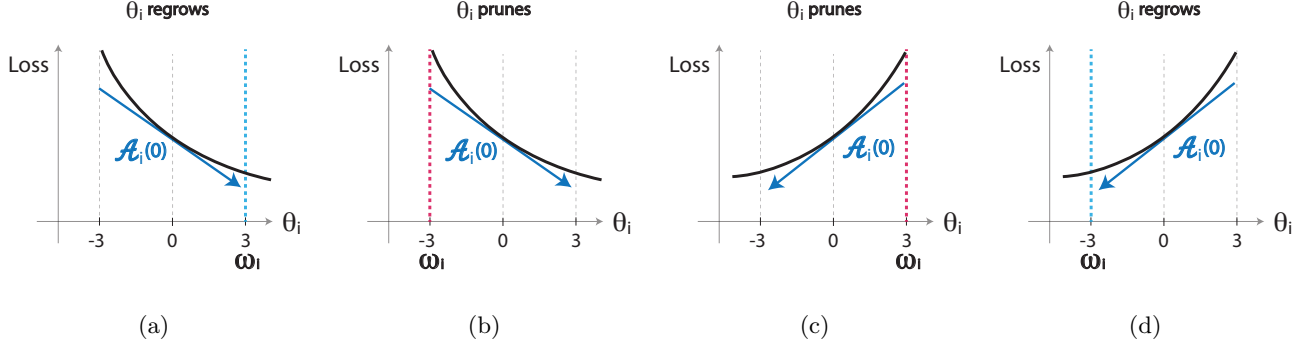


Figure 1: Scenarios for θ_i when $H(t_i) = 0$. If \mathcal{A}_i points towards ω_i the flux \mathcal{G}_i^- regrows the weight as in (a) and (d). Otherwise, it keeps the weight pruned as in (b) and (c). Numerical values are only illustrative.

\mathcal{A}_i represents the direction in which the effective weight θ_i should change to minimize the loss. If \mathcal{A}_i has the same sign as the weight ω_i , then t_i will increase, reinforcing presence. Otherwise, if they have different signs, t_i will decrease towards pruning. This behavior takes two meanings depending on whether $t_i \leq 0$ or $t_i > 0$, which we analyze below. For this purpose, we define $\mathcal{W}_i = -\frac{\partial \mathcal{L}}{\partial \omega_i}$, the direction in which ω_i should change to reduce the loss.

For $t_i > 0$, $\mathcal{W}_i = \mathcal{A}_i \cdot H(t_i) = \mathcal{A}_i$. Therefore, $\mathcal{G}_i(\omega, \mathcal{T})$ can be rewritten as $\mathcal{W}_i \cdot \omega_i$, meaning that t_i increases when \mathcal{W}_i and ω_i have the same sign and decreases otherwise. Note that \mathcal{W}_i and ω_i having the same sign also means that $|\omega_i|$ increases, while opposite signs imply that $|\omega_i|$ decreases. Therefore, t_i follows the direction of change in $|\omega_i|$.

To assess the importance of $\theta_i = \omega_i$, the method allows $t_i \leq 0$, causing $\theta_i = 0$, and checks whether as a result \mathcal{A}_i points towards ω_i , i.e. whether $\text{sign}(\mathcal{A}_i) = \text{sign}(\omega_i)$. If this is true, moving θ_i from 0 towards ω_i would reduce the new loss (obtained after θ_i became 0) and consequently, \mathcal{G}_i increases t_i until regrowth, $\theta_i = \omega_i$. In this way, Hyperflux implements the key insight that *one never knows the value of something (θ_i) until one loses it (sets it to 0)*. Otherwise, if $\text{sign}(\mathcal{A}_i) \neq \text{sign}(\omega_i)$, t_i decreases, keeping the weight pruned, $\theta_i = 0$. All four combinations of signs are presented in Fig. 1. For this $t_i \leq 0$ setting, \mathcal{G}_i takes the meaning of *flux*, and its relation to weight importance is further discussed in Appendix A.2.

Given the fact that $\mathcal{G}_i(\omega, \mathcal{T})$ takes two different meanings, we introduce two different notations:

$$\mathcal{G}_i(\omega, \mathcal{T}) =: \begin{cases} \mathcal{G}_i^-(\omega, \mathcal{T}), & t_i \leq 0, \\ \mathcal{G}_i^+(\omega, \mathcal{T}), & t_i > 0. \end{cases} \quad (2)$$

$\mathcal{G}_i^-(\omega, \mathcal{T})$ refers to flux, whereas $\mathcal{G}_i^+(\omega, \mathcal{T})$ is the tendency of $|\omega_i|$.

Despite having flux as a metric of importance, we have

not presented so far a criterion to prune the weights, that would lead us to uncover their flux. To drive t values towards $-\infty$, we employ an “ $L_{-\infty}$ ” loss called *pressure*, formulated as:

$$L_{-\infty}(t) = \frac{1}{d} \cdot \gamma \cdot \sum_{i=1}^d t_i, \quad (3)$$

where γ is a scalar used to control sparsity and d the total number of weights in the network. Any reference about an increase, decrease, value or scheduler of pressure will refer to γ . The pressure term yields a constant gradient $\frac{\gamma}{d}$ with respect to each t_i parameter, independent of their current value.

In Appendix A.1, we analyze Hyperflux mechanics in more detail, and show that a weight will be regrown only if the average flux is greater than the pressure for the training interval in which the weight is pruned. Since flux only exists if weights encode meaningful information, we begin pruning by initializing the network with *pretrained weights*.

3.3 Minimum Flux and Convergence

Following from the insights about flux and pressure described so far, we postulate a series of properties that naturally emerge. We experimentally validate each of the properties, confirming our expectations, and laying the foundation for the *Neural Pruning Law Hypothesis*.

Property 1: Density Convergence for a Fixed γ . As density decreases, fewer weights are used to represent the same information contained within the dataset. As long as the accuracy remains constant, the importance – and therefore flux – of the remaining weights should increase. Once the minimum flux among all weights, \mathcal{W}_f , matches the pressure, we expect density to converge to an equilibrium. Therefore, we ask the following question: *Given a fixed γ , will the network converge to a final density \mathcal{D} ?* In Figure 2, we test

this by running ResNet-50 and VGG-19 on Cifar-10, Cifar-100 respectively. We preload weights for each network and allow it to train for 1000 epochs with a constant pressure γ .

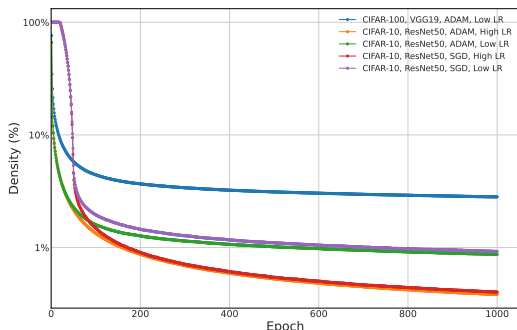


Figure 2: Convergence for fixed $\gamma = 2$.

To better understand how convergence is affected by optimizers and learning, we test two different optimizers for t values, SGD and Adam, along with a high and low learning rate, differing by two orders of magnitude. We observe that networks with low learning rates tend to converge faster and smoother compared to high learning rates. Further ablation studies are found in Appendix B.

Property 2: Relationship Between Minimum Weight Flux and Density. Property 1 says that all networks converge to a fixed density for a fixed γ , when $\mathcal{W}_f = \gamma$, and do not end up diverging or oscillating. Therefore, we ask: *Is there a predictable relationship between minimum flux among weights and network density?* For each experiment, we train a network with constant γ and allow it to converge. The learning rate is kept constant, since it influences the final density (see Fig 2). Figure 3 illustrates different convergence points for several γ values for ResNet-50, Cifar-10. Similar results can be seen in Appendix C.1 for VGG-19, Cifar-100.

We observe three regions taking shape in our experiments. In region 1, the pressure is too small for any meaningful weights to be pruned and information compression to occur. In region 2, we observe constant accuracy over a large density range, where meaningful information compression occurs, leading to a clear power-law relationship between pressure and density!

$$\ln(s) = \ln(c) - \alpha_0 \ln(\gamma) \quad (4)$$

where constants, c , α_0 , depend on dataset and network architecture. In region 3, where accuracy starts collapsing along with the remaining weights, leading eventually to 0% density. Our *Neural Pruning Law Hypothesis* will be concerned with region 2.

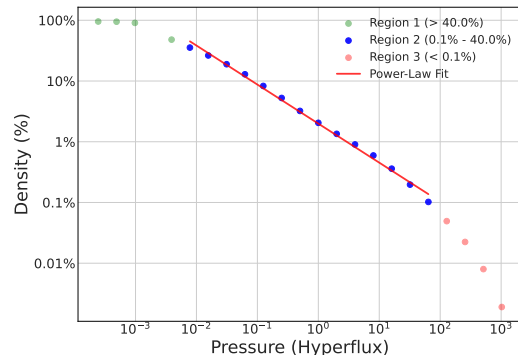


Figure 3: The relationship between γ (minimum flux) and final density for ResNet-50, Cifar-10. The 3 regions we discussed are highlighted in the figure.

3.4 The Neural Pruning Law Hypothesis

Our analysis in Section 3.2 showed that weight flux is an effective pruning criterion and that, according to Property 2, the relationship between \mathcal{W}_f and density follows a power-law. We hypothesize that such a power-law relationship holds for ANY effective saliency measure, including most pruning methods heuristics. We denote this idea as the *Neural Pruning Law Hypothesis* (NPLH). While fully validating NPLH is left for future work, we provide a strong preliminary set of experiments. We include 3 types of pruning methods: magnitude pruning, represented by iterative magnitude pruning (Frankle and Carbin, 2019), gradient-based methods, represented by Taylor approximation, (Molchanov et al., 2019) and L_0 methods, represented by Hyperflux.

We run the 3 methods on combinations of Cifar-10, Cifar-100 and ImageNet datasets with ResNet-50 and VGG-19 networks, and expect to see the same 3 regions along with the power-law appear for any importance approximation. As a common baseline, we choose ResNet-50 on Cifar-10, as it is implemented in all method we chose. The training setup for NPLH is detailed in Appendix C.1. Figure 4 includes results for ResNet-50 Cifar-10 for all 3 methods. The power-law region is highlighted for each method. Further studies on VGG-19 and ResNet-50 networks trained on Cifar-100 and ImageNet are also included Appendix C.1 and display the same 3 regions.

A likely explanation for the fact that all reasonable measures of saliency follow the power law is that all these measure approximate some fundamental importance of the weights. What that importance is exactly, remains to be seen in future work.

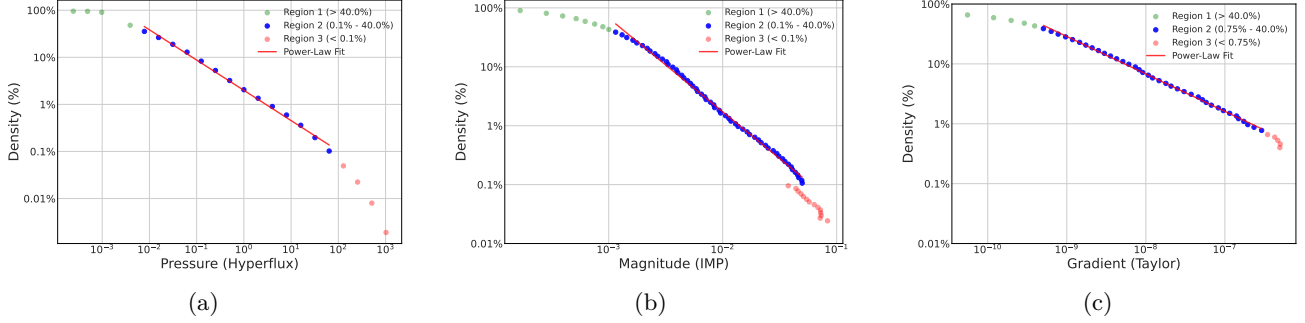


Figure 4: The relationship between minimum saliency among weights and density, for ResNet-50 (Cifar-10 on Hyperflux (representing L_0 methods), Iterative magnitude pruning and Taylor approximation (representing gradient methods)). The 3 regions as well as the power-law relation are clearly delimited in all 3 cases.

3.5 Pressure Scheduler & Stabilization Stage

Our findings from Section 3.3 suggest that a γ exists for any desired \mathcal{D} . However, in practical applications, γ is not known at the start and tuning it would require hyperparameter search. Instead, we propose a dynamic scheduler that adjusts γ after each epoch automatically, driving the network towards a desired sparsity. Furthermore, to ensure convergence of weights after pruning, we introduce a stabilization stage at the end.

Algorithm 1 Pressure scheduler - SCHED(s_e, e)

- 1: **Input:** Current sparsity d_e and epoch e
 - 2: **Requires:** Pruning epochs E_p , desired final sparsity \mathcal{D} , pressure policy Π , step u , exponent α .
 - 3: **Internals:** Positive and negative inertia p_+, p_- , base scalar p_e for epoch 1, p_1 (all initialized to 0).
 \triangleright Runs after each epoch
 - 4: **if** $\Pi(E_p, \mathcal{D}, d_e, e)$ **then**
 - 5: $p_e \leftarrow p_{e-1} + u + p_+$
 - 6: $p_+ \leftarrow p_+ + \frac{u}{4}$
 - 7: $p_- \leftarrow 0$
 - 8: **else**
 - 9: $p_e \leftarrow p_{e-1} - u - p_-$
 - 10: $p_- \leftarrow p_- + \frac{u}{4}$
 - 11: $p_+ \leftarrow 0$
 - 12: **end if**
 - 13: **Return:** pressure $\gamma_e = (p_e)^\alpha$
-

Pressure Scheduler: The goal of our scheduler is to adjust γ such that the network converges to \mathcal{D} with minimal accuracy decrease. We denote by γ_e and d_e , the pressure and network density at epoch e . Because the frequency of updates is constant, occurring after each epoch, any non-linear change in pressure required to affect density (see Eq. 4) must arise from the update rule. To get this nonlinearity we set $\gamma_e = (p_e)^\alpha$, with p_e , a scalar base, updated according to Algorithm 1. Inertia terms p_+ and p_- account for suboptimal α or u . Apart from non-linear updates, our scheduler requires a binary pressure policy Π to determine when those updates are applied such that \mathcal{D} is reached. We

explore two choices for Π . In the first, d_e follows a user-defined curve $f(e)$, trading precise convergence to \mathcal{D} for trajectory control. In this case $\Pi(E_p, \mathcal{D}, d_e, e)$ is true if and only if $d_e < f(e)$. In the second policy, d_e stays between a dynamic upper bound and the target \mathcal{D} , achieving precise convergence to \mathcal{D} at the cost of poorer trajectory control. Both policies are discussed in Appendix E.

Stabilization Stage: One side effect of Hyperflux is the noise created by pruning and reactivation of weights, which while helpful for pruning, is harmful for convergence. For this reason, to allow the weights and network topology to converge, we introduce a stabilization stage. Specifically, we set the pressure to zero to encourage regrowth while simultaneously decaying the learning rate η_t to prevent excessive reactivation.

Algorithm 2 Hyperflux Pruning Algorithm

- 1: **Input:** Pretrained weights ω^{init} , pruning epochs E_p , stabilization epochs E_s (leading to total epochs $E_t = E_p + E_s$), pressure scheduler SCHED(d_e, e).
 - 2: **Output:** Weights ω^* , final topology \mathcal{T}^* .
 - 3: **Initialize:**
 - 4: Weights $\omega \leftarrow \omega^{\text{init}}$.
 - 5: Presence parameters $t_i \leftarrow$ positive values, $\forall i \in \{1, 2, \dots, d\}$.
 - 6: Topology $\mathcal{T}_i \leftarrow 1, \forall i \in \{1, 2, \dots, d\}$.
 - 7: **for** epoch $e = 1$ to E_t **do**
 - 8: Calculate total loss $\mathcal{J}(\omega, \mathcal{T}) = \mathcal{L}(\omega, \mathcal{T}) + L_\infty(t)$.
 - 9: $\omega \leftarrow \omega - \eta_\omega \nabla_\omega \mathcal{L}$.
 - 10: $t \leftarrow t - \eta_t \nabla_t \mathcal{J}$.
 - 11: **if** $e \leq E_p$ **then**
 - 12: $\gamma \leftarrow$ SCHED(current density d_e, e)
 - 13: **else**
 - 14: $\eta_t \leftarrow 0.9 \cdot \eta_t$
 - 15: $\gamma \leftarrow 0$
 - 16: **end if**
 - 17: **end for**
-

Table 1: Comparison on CIFAR-10 and CIFAR-100 datasets at different pruning ratios (90.0%, 95.0%, 98.0%). Bold values represent the best performance for each setting.

Dataset	CIFAR-10			CIFAR-100		
	90.0%	95.0%	98.0%	90.0%	95.0%	98.0%
VGG-19 (Dense)	93.85 ± 0.06			73.44 ± 0.09		
SNIP*	93.63	93.43	92.05	72.84	71.83	58.46
GraSP*	93.30	93.04	92.19	71.95	71.23	68.90
Synflow*	93.35	93.45	92.24	71.77	71.72	70.94
GMP	93.82 ± 0.15	93.84 ± 0.14	92.34 ± 0.13	73.57 ± 0.20	73.39 ± 0.11	72.78 ± 0.07
RigL	93.60±0.15	93.17±0.09	92.39 ± 0.04	73.03±0.14	72.68±0.22	70.02 ± 0.7
GraNet ($s_i = 0$)	93.87 ± 0.05	93.84 ± 0.16	93.87 ± 0.11	74.08 ± 0.10	73.86 ± 0.04	73.00 ± 0.18
Hyperflux (ours)	94.05 ± 0.17	94.15 ± 0.14	93.95 ± 0.18	74.37 ± 0.21	74.18 ± 0.15	72.9 ± 0.05
ResNet-50 (Dense)	94.72 ± 0.05			78.32 ± 0.08		
SNIP*	92.65	90.86	87.21	73.14	69.25	58.43
GraSP*	92.47	91.32	88.77	73.28	70.29	62.12
Synflow*	92.49	91.22	88.82	73.37	70.37	62.17
RigL	94.02±0.33	93.76±0.23	92.93 ± 0.1	78.04±0.19	77.39±0.21	75.61 ± 0.11
GMP	94.81 ± 0.05	94.89 ± 0.1	94.52 ± 0.12	78.39 ± 0.18	78.38 ± 0.43	77.16 ± 0.25
GraNet ($s_i = 0$)	94.69 ± 0.08	94.44 ± 0.01	94.34 ± 0.17	79.09 ± 0.23	78.71 ± 0.16	78.01 ± 0.20
Hyperflux (ours)	95.41 ± 0.12	95.15 ± 0.11	95.26 ± 0.13	79.58 ± 0.18	79.23 ± 0.16	77.7 ± 0.08

4 Hyperflux Performance

We now show that Hyperflux, in addition to allowing us to come up with NPLH, also has strong empirical performance. To validate *Hyperflux*, we conduct comprehensive pruning experiments on a diverse set of architectures and datasets: ResNet-50 and VGG-19 on CIFAR-10/100, and ResNet-50 on ImageNet-1K. We pit Hyperflux against state-of-the-art pruning approaches such as GraNet Liu et al. (2022), GMP Zhu and Gupta (2018), Spartan Tai et al. (2022), and AC/DC Peste et al. (2021). To ensure a fair comparison, we run ourselves all other methods, initializing them with the pretrained weights used in Hyperflux, while maintaining the same training budget and augmentations. We test several training setups for each method and report the best results, to ensure no unfair degradation occurs due to suboptimal hyperparameters.

Additionally, to better position Hyperflux within the broader literature, we choose to include one-shot methods Lee et al. (2019); Wang et al. (2020); Tanaka et al. (2020) commonly used as benchmarks in other works, even though our post-training setup is not applicable to them. These benchmarks will be marked with *.

None of our comparison methods incorporate learnable masks as Hyperflux does. Although we identified some mask-based methods Savarese et al. (2020); Louizos et al. (2018); Zhang et al. (2022), their differences in benchmarks, methodology or missing code prevent a direct comparison to our work. Each configuration but ResNet-50 on ImageNet is run three times and

we report the results as mean ± standard deviation, all experiments are run on three NVIDIA GeForce RTX 4090 GPUs. Full details on training recipe are in Appendix F.

4.1 CIFAR-10 / 100

We evaluate the performance of *Hyperflux* on CIFAR-10 and CIFAR-100 using ResNet-50 and VGG-19 architectures. Results are presented in Table 1. On CIFAR-10, *Hyperflux* outperforms the baseline at 90%, 95%, and 98% sparsity for both VGG-19 and ResNet-50, with accuracy gains under 1% over the next best. Specifically, for VGG-19, it beats GraNet by 0.18% and GMP by 0.23% at 90% sparsity (rising to 1.61% over GMP at 98%), while on ResNet-50 it maintains a 0.7% lead over GraNet across all levels. We also analyze ResNet-50’s layer-wise sparsity at extreme rates (99.74%, 99.01%, 98.13%) and illustrate weight distribution changes in Appendix C.2.

On CIFAR-100, *Hyperflux* leads in 4 of 6 benchmarks, being behind GraNet by only 0.1% and 0.3% in the other two. Notably, GraNet gains nearly 2% on ResNet-50 when initialized with our pretrained weights. Conversely, RigL gains 1.5% points of accuracy on ResNet-50 for CIFAR-100, yet experiences drops of up to 0.3% on ResNet-50 for CIFAR-10. On the remaining two benchmarks, its gains are only moderate. At 90% and 95% sparsity, *Hyperflux* outperforms all methods, including GraNet, by 0.5%. Furthermore, GMP finds itself at a difference of 0.2% at 98% sparsity on VGG-19, increasing to 1.2% points of accuracy at 90% sparsity,

while RigL is behind by 2.9% at 98% and 1.3% at 90% sparsity.

4.2 ImageNet-2012

To test *Hyperflux* at scale, we pruned ResNet-50 on ImageNet-2012. Table 2 shows that, even at extreme sparsity, *Hyperflux* performs competitively against state-of-the-art. Interestingly, our loading of pretrained weights increased the accuracy of all methods, with the exception of Spartan, which lost almost 1.5% accuracy compared to its reported results.

At 96.42% sparsity, *Hyperflux* reaches 72.21% accuracy, surpassing GMP, GraNet and Spartan, while performing competitively against AC/DC, at a difference of 0.3%. This hierarchy is maintained for both

Table 2: ResNet-50 top-1 accuracy, parameter count, sparsity, and compute cost on ImageNet-2012. We denote by s the sparsity, and by F_{train} and F_{test} the compute cost (FLOPs) required for training and testing, respectively.

Method	Top-1(%)	Params	s(%)	F_{test}	F_{train}
ResNet-50	77.01	25.6M	0.00	1.00×	1.00×
GMP	74.29	2.56M	90.00	0.10×	0.51×
GraNet	74.68	2.56M	90.00	0.16×	0.23×
Spartan	75.12	2.56M	90.00	0.14×	-
AC/DC	75.83	2.56M	90.00	0.18×	0.58×
Hyperflux	75.28	2.54M	90.11	0.15×	0.60×
GMP	70.95	1.28M	95.00	0.05×	-
GraNet	72.83	1.28M	95.00	0.12×	0.17×
Spartan	72.92	1.28M	95.00	0.08×	-
AC/DC	74.03	1.28M	95.00	0.11×	0.53×
Hyperflux	73.30	1.28M	95.00	0.08×	0.52×
GMP	70.62	0.90M	96.50	-	-
GraNet	71.06	0.90M	96.50	0.09×	0.15×
Spartan	71.13	0.90M	96.50	-	-
AC/DC	72.50	0.90M	96.50	-	-
Hyperflux	72.21	0.92M	96.42	0.06×	0.49×

90% and 95% sparsity, with the gap between Hyperflux and AC/DC remaining below 0.6 points in accuracy. We conducted an analysis on the weight histograms of ResNet-50 on ImageNet to study the difference in weight distribution and observed that Hyperflux pruned aggressively the convolutional layers, details in Appendix C.2

The computational cost is only assessed on ImageNet-1k as it is the most intensive benchmark. Pruning cuts FLOPs to 0.15× inference/0.60× training at 90% sparsity, and 0.08×/0.52× at 95% sparsity. Despite incurring larger costs for training than other methods, Hyperflux is able to produce sparse networks whose

inference cost is lower. This is caused by the per-layer sparsity distribution generated by our method, which prunes more the layers contributing most to the computational cost. For the baselines, we report the computational costs when they are available in their respective papers, and fill with – when they are not. More details on computational cost are given in Appendix D.

5 Conclusions

We introduced Hyperflux, a conceptually grounded L_0 method in which we construct the notions of flux and pressure and study their relationship with weight importance. Furthermore, we postulate and validate several properties of Hyperflux, leading us to the Neural Pruning Law Hypothesis, a general property for neural pruning.

In future works, we plan on extending the experiments validating NPLH, to natural language processing, generative modelling and reinforcement learning. Furthermore, we want to test a wider range of architectures such as recurrent neural networks and transformers.

References

- Réka Albert, Hawoong Jeong, and Albert-László Barabási. Error and attack tolerance of complex networks. *Nature*, 2000.
- Zeyuan Allen-Zhu, Yuanzhi Li, and Zhao Song. A Convergence Theory for Deep Learning via Over-Parameterization. In *International Conference on Machine Learning*, 2019.
- Guillaume Bellec, David Kappel, Wolfgang Maass, and Robert Legenstein. Deep Rewiring: Training Very Sparse Deep Networks. In *International Conference on Learning Representations*, 2018.
- Minho Cho, Sanjaya Adya, and Dattaraj Naik. PDP: Parameter-Free Differentiable Pruning is All You Need. In *International Conference on Neural Information Processing Systems*, 2023.
- Pau De Jorge, Amartya Sanyal, Harkirat Singh Behl, Philip HS Torr, Grégory Rogez, and Puneet Kumar Dokania. Progressive Skeletonization: Trimming More Fat from a Network at Initialization. In *International Conference on Learning Representations*, 2021.
- Utku Evci, Gale, Trevor, Menick, Jacob, Castro, Pablo Samuel, and Erich Elsen. Rigging the Lottery: Making All Tickets Winners. In *International Conference on Machine Learning*, 2020.
- Jonathan Frankle and Michael Carbin. The Lottery Ticket Hypothesis: Finding Sparse, Trainable Neural

- Networks. In *International Conference on Learning Representations*, 2019.
- Elias Frantar, Carlos Riquelme Ruiz, Neil Houlsby, Dan Alistarh, and Utku Evci. Scaling Laws for Sparsely-Connected Foundation Models. In *International Conference on Learning Representations*, 2024.
- Athanasios Glentis Georgoulakis, George Retsinas, and Petros Maragos. Feather: An Elegant Solution to Effective DNN Sparsification. In *34th British Machine Vision Conference*, 2023.
- Guri Giaefer, Angela M. Chu, Li Ni, Carla Connelly, Linda Riles, Steeve Véronneau, and et al. Functional profiling of the *Saccharomyces cerevisiae* genome. *Nature*, 2002.
- Song Han, Jeff Pool, John Tran, and William Dally. Learning Both Weights and Connections for Efficient Neural Network. In *International Conference on Neural Information Processing Systems*, 2015.
- Song Han, Huizi Mao, and William Dally. Deep compression: Compressing Deep Neural Networks with Pruning, Trained Quantization and Huffman Coding. In *International Conference on Learning Representations*, 2016.
- Torsten Hoefer, Dan Alistarh, Tal Ben-Nun, Nikoli Dryden, and Alexandra Peste. Sparsity in Deep Learning: Pruning and growth for efficient inference and training in neural networks. *Journal of Machine Learning Research*, 2021.
- Gaojie Jin, Xinpeng Yi, Liang Zhang, Lijun Zhang, Sven Schewe, and Xiaowei Huang. How does Weight Correlation Affect the Generalisation Ability of Deep Neural Networks? In *Advances in Neural Information Processing Systems*, 2020.
- Park Jongsoo, Li Sheng, Wen Wei, Tak Ping, Li Hai, Chen Yiran, and Dubey Pradeep. Faster CNNs with Direct Sparse Convolutions and Guided Pruning. In *International Conference on Learning Representations*, 2017.
- Aditya Kusupati, Vivek Ramanujan, Raghav Somani, Mitchell Wortsman, Prateek Jain, Sham Kakade, and Ali Farhadi. Soft Threshold Weight Reparameterization for Learnable Sparsity. In *International Conference on Machine Learning*, 2020.
- Yann LeCun, John S Denker, and Sara A Solla. Optimal Brain Damage. In *International Conference on Neural Information Processing Systems*, 1989.
- Yann LeCun, John S Denker, and Sara A Solla. Second Order Derivatives for Network Pruning: Optimal Brain Surgeon. In *International Conference on Neural Information Processing Systems*, 1992.
- Jason Lee, Jie Gao, Cho-Jui Hsieh, and Tal Hassner. SNIP: Single-shot Network Pruning based on Connection Sensitivity. In *International Conference on Learning Representations*, 2019.
- Chunyuan Li, Heerad Farkhoor, Rosanne Liu, and Jason Yosinski. Measuring the Intrinsic Dimension of Objective Landscapes. In *International Conference on Learning Representations*, 2018.
- En Li, Zhi Zhou Liekang Zeng, and Xu Chen. Edge AI: On-demand accelerating deep neural network inference via edge computing. *IEEE Transactions on Wireless Communications*, 2019.
- Zhuohan Li, Eric Wallace, Sheng Shen, Kevin Lin, Kurt Keutzer, Dan Klein, and Joseph E. Gonzalez. Train Big, Then Compress: Rethinking Model Size for Efficient Training and Inference of Transformers. In *International Conference on Machine Learning*, 2020.
- Tao Lin, Sebastian U. Stich, Luis Barba, Daniil Dmitriev, and Martin Jaggi. Dynamic Model Pruning with Feedback. In *Proceedings of the International Conference on Learning Representations (ICLR)*, 2020.
- Junjie Liu, Zhe Xu, Runbin Shi, Ray Cheung, and Hayden So. Dynamic Sparse Training: Find Efficient Sparse Network From Scratch With Trainable Masked Layers. *arXiv:2005.06870*, 2020.
- Shiwei Liu, Tianlong Chen, Xiaohan Chen, Zahra Atashgahi, Lingfei Yin, Haizhao Kou, Li Shen, Mykola Pechenizkiy, and Zhangyang Wang. Sparse Training via Boosting Pruning Plasticity with Neuroregeneration. In *International Conference on Neural Information Processing Systems*, 2022.
- Christos Louizos, Karen Ullrich, and Max Welling. Bayesian Compression for Deep Learning. In *31st Conference on Neural Information Processing Systems*, 2017.
- Christos Louizos, Max Welling, and Diederik P. Kingma. Learning Sparse Neural Networks Through L_0 Regularization. In *International Conference on Learning Representations*, 2018.
- Xiaolong Ma, Geng Yuan, Xuan Shen, Tianlong Chen, Xuxi Chen, Xiaohan Chen, Ning Liu, Minghai Qin, Sijia Liu, Zhangyang Wang, and Yanzi Wang. Sanity Checks for Lottery Tickets: Does Your Winning Ticket Really Win the Jackpot? In *International Conference on Neural Information Processing Systems*, 2021.
- Pavlo Molchanov, Arun Mallya, Stephen Tyree, Iuri Frosio, and Jan Kautz. Importance Estimation for Neural Network Pruning. In *Proceedings of the IEEE/CVF Conference on Computer Vision and Pattern Recognition (CVPR)*, 2019.

- Michael C. Mozer and Paul Smolensky. Skeletonization: A Technique for Trimming the Fat from a Network via Relevance Assessment. In *International Conference on Neural Information Processing Systems*, 1988.
- Behnam Neyshabur, Zhiyuan Li, Srinadh Bhojanapalli, Yann LeCun, and Nathan Srebro. The role of over-parametrization in generalization of neural networks. In *International Conference on Learning Representations*, 2019.
- Alexandra Peste, Eugenia Iofinova, Adrian Vladu, and Dan Alistarh. AC/DC: Alternating Compressed/DeCompressed Training of Deep Neural Networks. In *Advances in Neural Information Processing Systems*, 2021.
- Vivek Ramanujan, Mitchell Wortsman, Aniruddha Kembhavi, Ali Farhadi, and Mohammad Rastegari. What’s Hidden in a Randomly Weighted Neural Network? In *Proceedings of the IEEE/CVF Conference on Computer Vision and Pattern Recognition*, 2020.
- Chris Rorden and Hans-Otto Karnath. Using lesion-symptom mapping to study brain function. *Journal of Cognitive Neuroscience*, 2004.
- Pedro Savarese, Hugo Silva, and Michael Maire. Winning the Lottery with Continuous Sparsification. In *International Conference on Neural Information Processing Systems*, 2020.
- Ophir Shalem, Neville E. Sanjana, Ella Hartenian, Xi Shi, David A. Scott, Tarjei S. Mikkelsen, Dirk Heckl, Benjamin L. Ebert, David E. Root, John G. Doench, and Feng Zhang. Genome-scale CRISPR-Cas9 knockout screening in human cells. *Science*, 2014.
- Weisong Shi, Jie Cao, Quan Zhang, Youhuizi Li, and Lanyu Xu. Edge Computing: Vision and Challenges. *IEEE Internet of Things Journal*, 2016.
- Sidak Pal Singh and Dan Alistarh. Efficient Second Order Derivatives for Network Compression. In *International Conference on Neural Information Processing Systems*, 2020.
- Kai Sheng Tai, Taipeng Tian, and Ser-Nam Lim. Spartan: Differentiable Sparsity via Regularized Transportation. In *Advances in Neural Information Processing Systems*, 2022.
- Hidegori Tanaka, Daniel Kunin, Daniel L. K. Yamins, and Surya Ganguli. Pruning neural networks without any data by iteratively conserving synaptic flow. In *Advances in Neural Information Processing Systems*, 2020.
- Adly Templeton, Tom Conerly, Jonathan Marcus, Jack Lindsey, Trenton Bricken, Brian Chen, Adam Pearce, Craig Citro, Emmanuel Ameisen, Andy Jones, Hoagy Cunningham, Nicholas L Turner, Callum McDougall, Monte MacDiarmid, Alex Tamkin, Esin Durmus, Tristan Hume, Francesco Mosconi, C. Daniel Freeman, Theodore R. Sumers, Edward Rees, Joshua Batson, Adam Jermyn, Shan Carter, Chris Olah, and Tom Henighan. Scaling Monosemanticity: Extracting Interpretable Features from Claude 3 Sonnet. Technical report, Anthropic, 2024.
- Samuel Thimm and Hannes Hoppe. Evaluating Pruning Methods. In *Proceedings of the International Joint Conference on Artificial Intelligence*, 1995.
- Chaoqi Wang, Guodong Zhang, and Roger Grosse. Picking winning tickets before training by preserving gradient flow. In *International Conference on Learning Representations*, 2020.
- Kangning Wang, Zhuang Liu, Yujun Lin, Ji Lin, and Song Han. HAQ: Hardware-Aware Automated Quantization with Mixed Precision. In *Proceedings of the IEEE/CVF Conference on Computer Vision and Pattern Recognition (CVPR)*, 2019.
- Qihan Wang, Chen Dun, Fangshuo Liao, Chris Jermaine, and Anastasios Kyrillidis. LOFT: Finding Lottery Tickets through Filter-wise Training. In *Proceedings of the 26th International Conference on Artificial Intelligence and Statistics*, 2023.
- Mitchell Wortsman, Ali Farhadi, and Mohammad Rastegari. Discovering Neural Wirings. In *International Conference on Neural Information Processing Systems*, 2019.
- Xia Xiao, Zigeng Wang, and Sanguthevar Rajasekaran. AutoPrune: Automatic Network Pruning by Regularizing Auxiliary Parameters. In *International Conference on Neural Information Processing Systems*, 2019.
- Wang Yite, Li Dawei, and Sun Ruoyu. NTK-SAP: Improving neural network pruning by aligning training dynamics. *arXiv:2304.02840*, 2023.
- Yuxin Zhang, Mingbao Lin, Mengzhao Chen, Fei Chao, and Rongrong Ji. OptG: Optimizing Gradient-driven Criteria in Network Sparsity. *arXiv:2201.12826*, 2022.
- Hattie Zhou, Janice Lan, Rosanne Liu, and Jason Yosinski. Deconstructing Lottery Tickets: Zeros, Signs, and the Supermask. In *International Conference on Neural Information Processing Systems*, 2019.
- Michael Zhu and Suyog Gupta. To Prune, or Not to Prune: Exploring the Efficacy of Pruning for Model Compression. In *International Conference on Learning Representations*, 2018.

Checklist

1. For all models and algorithms presented, check if you include:
 - (a) A clear description of the mathematical setting, assumptions, algorithm, and/or model. Yes.
 - (b) An analysis of the properties and complexity (time, space, sample size) of any algorithm. Yes. We include complexity analysis in ablation studies as well as discussions within the main body for Hyperflux.
 - (c) (Optional) Anonymized source code, with specification of all dependencies, including external libraries. Yes.
2. For any theoretical claim, check if you include:
 - (a) Statements of the full set of assumptions of all theoretical results. Yes.
 - (b) Complete proofs of all theoretical results. Yes.
 - (c) Clear explanations of any assumptions. Yes.
3. For all figures and tables that present empirical results, check if you include:
 - (a) The code, data, and instructions needed to reproduce the main experimental results (either in the supplemental material or as a URL). Yes.
 - (b) All the training details (e.g., data splits, hyperparameters, how they were chosen). Yes.
 - (c) A clear definition of the specific measure or statistics and error bars (e.g., with respect to the random seed after running experiments multiple times). Yes.
 - (d) A description of the computing infrastructure used. (e.g., type of GPUs, internal cluster, or cloud provider). Yes.
4. If you are using existing assets (e.g., code, data, models) or curating/releasing new assets, check if you include:
 - (a) Citations of the creator If your work uses existing assets. Yes. Standard datasets (CIFAR-10/100, ImageNet-1K) and libraries (e.g., PyTorch) are used in compliance with their respective terms. CIFAR is available for research. ImageNet is used per its terms for non-commercial research, with images subject to original copyrights.
 - (b) The license information of the assets, if applicable. Yes.
 - (c) New assets either in the supplemental material or as a URL, if applicable. Not Applicable.
 - (d) Information about consent from data providers/curators. Not Applicable.
 - (e) Discussion of sensible content if applicable, e.g., personally identifiable information or offensive content. Not Applicable
5. If you used crowdsourcing or conducted research with human subjects, check if you include:
 - (a) The full text of instructions given to participants and screenshots. Not Applicable.
 - (b) Descriptions of potential participant risks, with links to Institutional Review Board (IRB) approvals if applicable. Not Applicable.
 - (c) The estimated hourly wage paid to participants and the total amount spent on participant compensation. Not Applicable.

Supplementary Material

A Analysis

A.1 Hyperflux mechanics

We let $\mathcal{G}_i(\omega, \mathcal{T})$ and the gradient of $L_{-\infty}(t)$ interact during backpropagation without direct intervention. As a result, a family of topologies $\mathcal{T}^{1 \rightarrow K}$ emerges *implicitly* during training by concurrent pruning (determined by $L_{-\infty}$) and regrowth (determined by \mathcal{G}_i^- increasing t_i). Furthermore, a $t_i \leq 0$ may be increased for several iterations until it reaches $t_i > 0$, being evaluated at each iteration over a potentially different topology $\mathcal{T}^k \in \mathcal{T}^{1 \rightarrow K}$. This behavior is desirable, given that evaluating flux on a single topology provides a limited estimate of importance. To get a better picture of the underlying interactions, we begin by extending equation (2) to a family of topologies:

$$\mathcal{G}_i^{-/+}(\omega, \mathcal{T}^{1 \rightarrow K}) = \frac{1}{K} \sum_{k=1}^K \mathcal{G}_i^{-/+}(\omega, \mathcal{T}^k). \quad (5)$$

This leads to an *aggregated flux* $\mathcal{G}_i^-(\omega, \mathcal{T}^{1 \rightarrow K})$ and an average tendency of change in weight magnitude $\mathcal{G}_i^+(\omega, \mathcal{T}^{1 \rightarrow K})$ respectively. In Hyperflux, the updates over H iterations write:

$$\sum_{h=1}^H \frac{\partial(\mathcal{L}(\mathcal{T}^h, \omega) + L_{-\infty}(t))}{\partial t_i} = \sum_{h=1}^H (\mathcal{G}_i(\omega, \mathcal{T}^h) + \frac{\gamma}{d}), \quad (6)$$

where \mathcal{T}^h is the topology at iteration h . We examine the “life cycle” of a presence parameter t_i over the H training iterations. In figure 5 we show how the gradients of t_i , represented by arrows, interact. During these H steps, t_i alternates between active phases during which it follows tendency of $|\omega_i|$, and pruned phases during which flux accumulates. We refer to the transition from a pruned phase back to a present phase as *implicit regrowth*. To illustrate the interactions between flux and pressure in our method, consider a pruned phase beginning at iteration P_s and ending at iteration P_f ($1 < P_s < P_f \leq H$). If P_f marks the final step of that pruned phase, the total change in t_i over $[P_s, P_f]$ is positive, which gives:

$$\sum_{h=P_s}^{P_f} (\mathcal{G}_i(\omega, \mathcal{T}^h) - \frac{\gamma}{d}) > 0 \quad (7)$$

If and only if:

$$(P_f - P_s) \cdot \left[\mathcal{G}_i^-(\omega, \mathcal{T}^{P_s \rightarrow P_f}) - \frac{\gamma}{d} \right] > 0. \quad (8)$$

Thus, a weight will be regrown if the aggregated flux is greater than the pressure. Conversely, after an active interval, the weight becomes pruned i.e. $\left[\mathcal{G}_i^+(\omega, \mathcal{T}^{P_s \rightarrow P_f}) - \frac{\gamma}{d} \right] < 0$. This mechanism influences all weights: pressure pushes them toward pruning, but they regrow whenever the aggregated flux exceeds that pressure. Consequently, since our method relies on weights that already encode meaningful information, we begin pruning by initializing the network with *pretrained weights*.

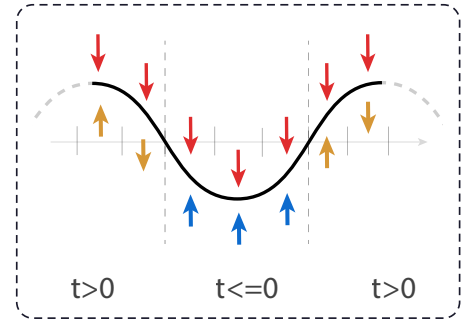


Figure 5: MNIST convergence for constant $\theta = 1$ for different learning rates

A.2 Why Important Weights Generate Stronger Flux

To study the flux of important weights, let us focus on a specific weight ω_i in the regime $t_i \leq 0$, and thus $\theta_i = 0$. For analytical purposes, we define the loss in terms of the effective weights $\theta_i = \omega_i \cdot H(t_i)$ as $\mathcal{L}(\theta)$, where $\mathcal{L}(\theta|\theta_i = 0)$ is the loss when $t_i \leq 0$ and $\mathcal{L}(\theta|\theta_i = \omega_i)$ is the loss when $t_i > 0$. We perform a Taylor expansion of $\mathcal{L}(\theta)$ around $\theta_i = 0$. By perturbing θ_i by ω_i (i.e. by approximating the effect of regrowing the weight), we observe that the first-order term in the expansion is the flux of ω_i . Formally:

$$\mathcal{L}(\theta|\theta_i = \omega_i) = \mathcal{L}(\theta|\theta_i = 0) + \omega_i \frac{\partial \mathcal{L}(\theta|\theta_i = 0)}{\partial \theta_i} + \frac{1}{2} \omega_i^2 \frac{\partial^2 \mathcal{L}(\theta|\theta_i = 0)}{\partial \theta_i^2} + O(\omega_i^3). \quad (9)$$

Recalling the formula for flux, $\mathcal{G}_i^-(\omega, \mathcal{T})$, and neglecting the second and higher-order terms:

$$\mathcal{L}(\theta|\theta_i = 0) - \mathcal{L}(\theta|\theta_i = \omega_i) \approx -\omega_i \frac{\partial \mathcal{L}(\theta|\theta_i = 0)}{\partial \theta_i} = \mathcal{G}_i^-(\omega, \mathcal{T}).$$

Thus we obtain a direct relationship between flux and weight importance: the flux approximates the change in the loss that could be incurred when the weight is regrown. However, this relationship holds only up to neglected higher-order terms, so it should be viewed as a useful approximation rather than an exact law.

A.3 Flux Connection To The Hessian

To relate flux to other importance metrics, specifically the Hessian, we consider the Taylor approximation from (9) and write:

$$\mathcal{L}(\theta|\theta_i = 0) - \mathcal{L}(\theta|\theta_i = \omega_i) = - \left(\omega_i \frac{\partial \mathcal{L}(\theta|\theta_i = 0)}{\partial \theta_i} + \frac{1}{2} \omega_i^2 \frac{\partial^2 \mathcal{L}(\theta|\theta_i = 0)}{\partial \theta_i^2} \right) - O(\omega_i^3).$$

Given that the flux $\mathcal{G}_i^-(\omega, \mathcal{T}) = -\omega_i \frac{\partial \mathcal{L}(\theta|\theta_i = 0)}{\partial \theta_i}$ and neglecting terms of order $O(\omega_i^3)$ and higher, we obtain:

$$\mathcal{L}(\theta|\theta_i = 0) - \mathcal{L}(\theta|\theta_i = \omega_i) \approx \mathcal{G}_i^-(\omega, \mathcal{T}) - \frac{1}{2} \omega_i^2 \underbrace{\frac{\partial^2 \mathcal{L}(\theta|\theta_i = 0)}{\partial \theta_i^2}}_{H_{ii}^\theta}$$

The second term, $-\frac{1}{2} \omega_i^2 H_{ii}^\theta$, contains the diagonal element, H_{ii}^θ , of the Hessian matrix of the loss function with respect to θ_i . This shows that our flux metric captures the linear component of the loss change, while the second term captures the quadratic component, which is generally associated with Hessian-based pruning methods like Optimal Brain Damage LeCun et al. (1989). In Optimal Brain Damage, a weight’s saliency is estimated by $\frac{1}{2} H_{ii} \omega_i^2$, typically under the assumption that the network is at a minimum where first-order gradients are zero. On the other hand, Hyperflux prunes the weights, therefore recovering the first linear component of the Taylor expansion which becomes 0 when weights converge.

B Ablation Studies

B.1 Factors influencing flux $\mathcal{G}_i^-(\omega, \mathcal{T})$

We begin by analyzing how the flux value $\mathcal{G}_i^-(\omega, \mathcal{T})$ is influenced by factors other than η_t , the learning rate on presence parameters. Our findings from Section 3.3, suggest that weight learning affects the behavior of flux, by changing the final convergence point a network will reach for the same constant pressure γ . We study this effect in the case of LeNet-300. We run the network for 1000 epochs for three different learning rates of 0.005, 0.0005 and 0.00005, with no schedulers used and the same constant γ . Our findings are summarized in Figure 6, which shows that increasing η_ω , the weights learning rate, leads to smaller fluxes and convergence at higher sparsities.

Given the impact of η_ω on network convergence, we study the influence of high and low learning rates on our pruning and regrowth phases. In our experiments, we study three setups on ResNet-50 with CIFAR-10. In the first two experiments, we study how constant learning rates across the entire pruning and regrowth process affect sparsity and regrowth. We choose a high learning rate of 0.01 and a low learning rate of 0.0001.

For our third experiment, we start with the high learning rate which is then decayed using cosine annealing to a low learning rate until the end of regrowth. For all three studies we let our scheduler guide the network towards the same sparsity rate of 1%. However, we observe significant differences in the regrowth stage. For the first experiment, regrowth does not occur at all, with more weights being pruned even after the pressure is set to 0, while for the low learning rate, the performance initially degrades, but is followed by a substantial regrowth stage where the number of remaining parameters increases by 60%. For the third experiment performance does not degrade as much as for the low learning rate and the regrowth is done in a more controlled way, experiencing an increase in remaining parameters of 35%. The results are illustrated in Figure 7.

Lastly, we study how weight flux is affected by weight decay. Being directly applied on the weights, weight decay acts on both pruned and present weights. If a weight has been pruned in the first epochs on the training, weight decay will keep making it smaller and smaller, in this way diminishing its flux. We run similar experiments to the ones before, with a learning rate of 0.01, decayed during training to 0.0001, both with and without the standard weight decay. As expected, we observe in Figure 9a that regrowth without weight decay is more ample. We run this experiment five times, and note that each time the pattern illustrated in the figure remains consistent.

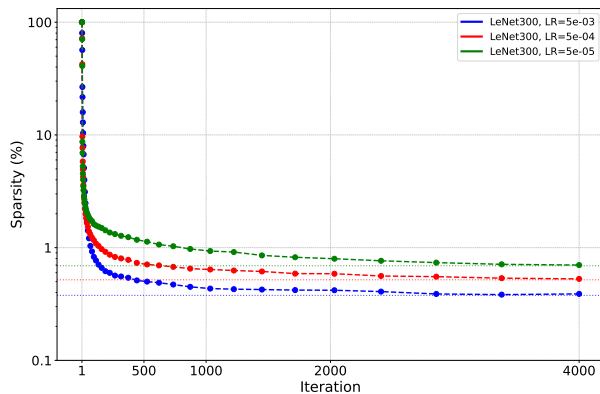
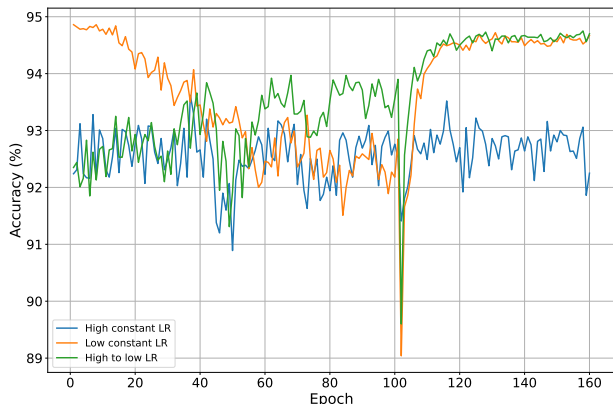
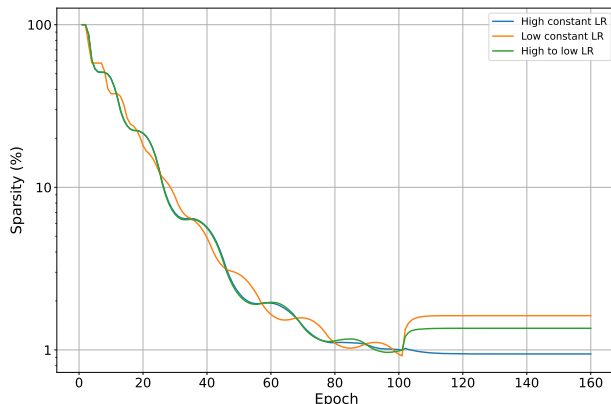


Figure 6: MNIST convergence for constant $\theta = 1$ for different learning rates



(a) Pruning accuracy vs. LR.



(b) Sparsity vs. LR.

Figure 7: The impact of the weights learning rate on pruning accuracy (left) and achieved sparsity (right).

B.2 Weights η_ω and pruning

Given the large impact η_ω has on flux, we explore its implications for producing an optimal pruning setup for Hyperflux. We run three experimental setups on ResNet-50 CIFAR-10 similar to the ones before. For each one of them, we select a starting learning rate, which is then decayed during training to 0.0001 to ensure convergence. For this setup, we run experiments using $\eta_\omega = 0.1, 0.01, 0.0001$. We analyze the results from the perspective of accuracy after pruning, noise, regrowth, and final accuracy. We find that the third setup is the most effective for Hyperflux.

We observe that each of the four studied aspects has a relationship with the learning rate. The noise is increased as initial learning rate increases, accuracy at the end of pruning is decreased the most for low learning rates and the highest for large learning rates. We obtain the highest final accuracy for higher learning rates and the regrowth phase is diminished the higher the learning rate. These relationships hold and can be easily seen in Figure 9.

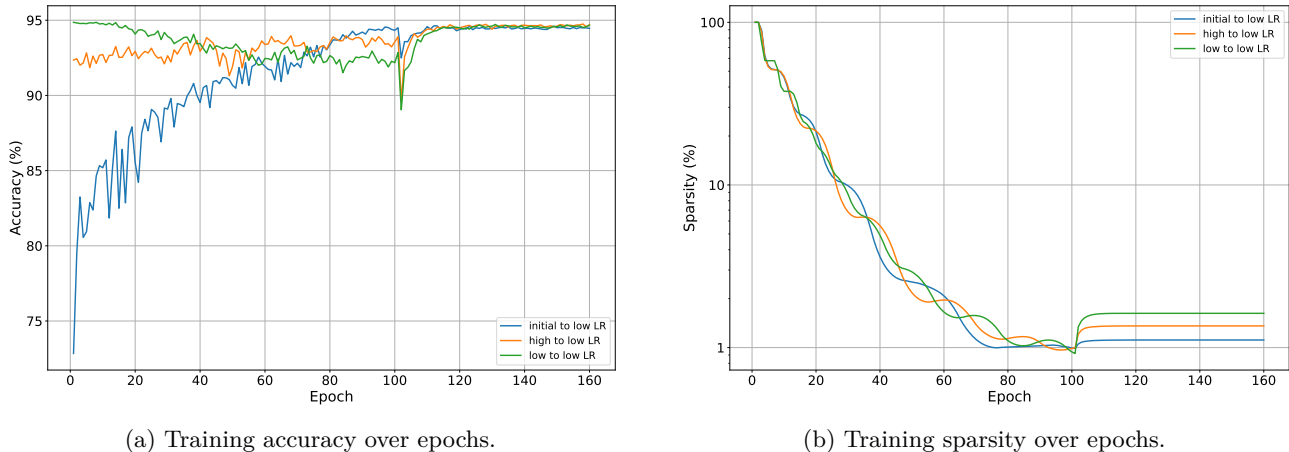


Figure 8: Training evolution for different learning rate configurations.

B.3 η_t values and regrowth

We analyze regrowth behavior for several values of η_t . At regrowth stage, we scale η_t with 5, 10, 20, 30 for VGG-19 on CIFAR-100 to observe the behavior of regrowth stage. Our findings are summarized in Figure 9b. As η_t increases so does the number of regrown weights. However, we note that after a point, generally about an increase of 50% in remaining parameters, the effects of regrowth start to be diminished and starts introducing noise in the performance, while also regrowing more weights.

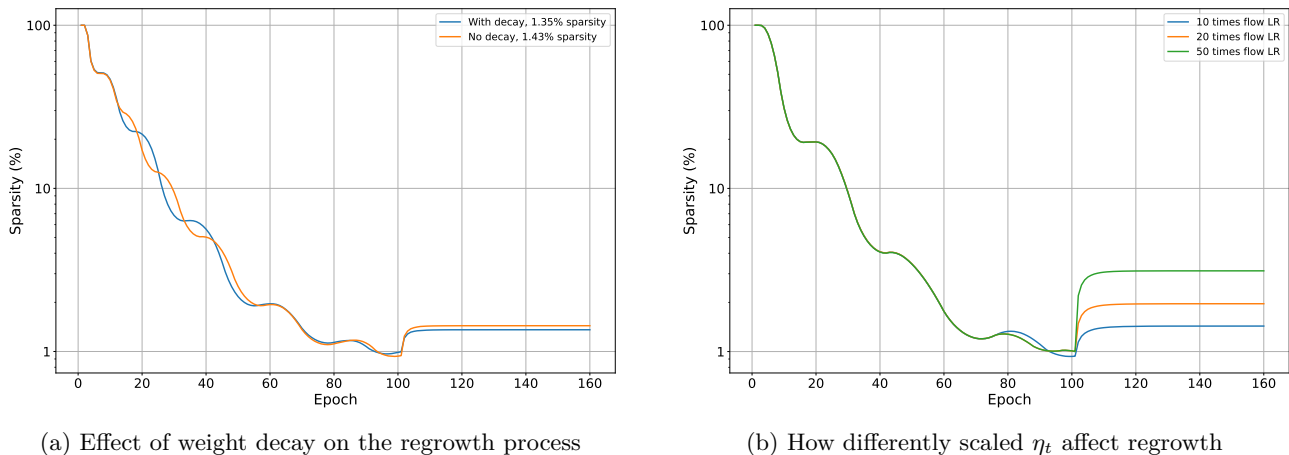


Figure 9: Factors affecting regrowth.

C Extended experiments

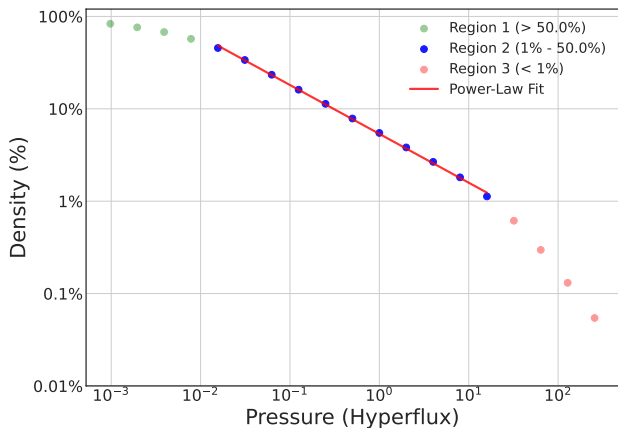
C.1 The Neural Pruning Law Hypothesis

We present extended experiments for the Neural Pruning Law Hypothesis, validating it on ImageNet-1K dataset and ResNet-50 network, as well as VGG-19 network and Cifar-100 dataset. We see that NPLH holds for several datasets and network architectures, as well as under different optimizers and learning rates. For VGG-19, Cifar-100 we see the three same distinct regions, also observed for ResNet-50, Cifar-10. However, for ImageNet, region 1 does not appear. This is natural for an under-parameterized network, struggling to learn the dataset, since there is not much redundancy within the network and compression occurs at all densities.

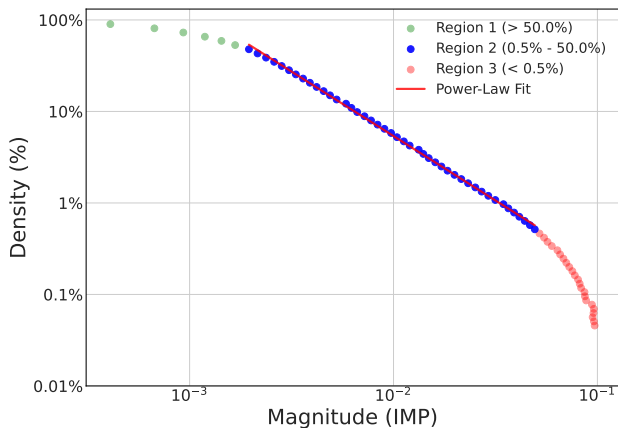
All experiments for NPLH were done by setting a constant learning rate for weights over the course of training and

preloading a trained network. For IMP and Taylor, we pruned 10% of the remaining weights at each 10 epochs, until accuracy of the network collapses and record the sparsity after each increase, along with the threshold value needed to prune 10% of remaining weights. We tested other types of training, such as directly increasing saliency cutoff, rather than pruning a % of weights and we observed the same results. The only difference appeared for region 3, which occurs earlier for flat saliency increase, due to its aggressivity at low densities.

For Hyperflux, we ran the setup from Property 2. We set an initial pressure in the beginning of the training and let the network converge for 300 epochs. We report the convergence sparsity produced by each pressure level and plot them, leading us to the same power-law.



(a) VGG-19, Cifar-100 on Hyperflux



(b) VGG-19, Cifar-100 on IMP

C.2 Layerwise sparsity levels & Weight Histograms

In this section, we examine the layer-wise sparsity observed for ResNet-50 on CIFAR-10 across the following pruning rates: 99.74%, 99.01%, and 98.13%. As illustrated in Figure 12, the overall sparsity hierarchy is maintained, displaying a decreasing trend in sparsity from the initial layers down to the final layer, where this pattern is interrupted. We hypothesize that earlier layers retain more weights due to their critical role in feature extraction, while deeper layers can sustain higher levels of pruning without significantly impacting overall performance. Notably, the penultimate layer experiences the highest degree of pruning, which means that it contains higher redundancy or less critical weights for performance. Furthermore, by analyzing the weight histograms for ResNet-50 with sparsity levels of 99.01% and 99.74% in Figure 15, we observe the influence of sparsity on the weight distributions. High sparsity levels significantly alter weight distributions, demonstrating that extreme pruning not only reduces the number of active weights but also changes the underlying weight dynamics within the network.

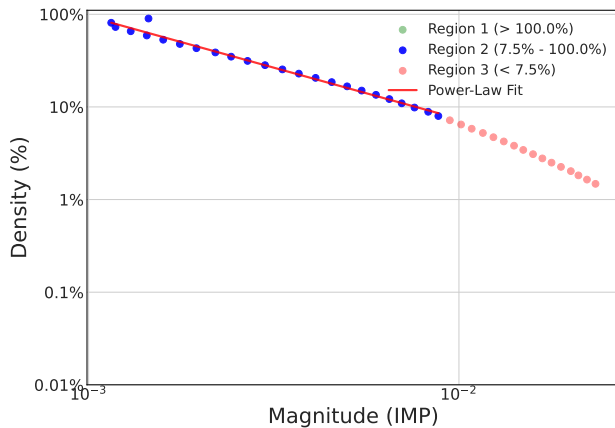


Figure 11: ResNet-50, ImageNet on IMP. Notice how region 1 does not appear, while the curvature of region 3 begins at higher sparsities, where accuracy begins degrading.

The histograms in Figure 16 illustrate the differences in weight distributions between the pruning and regrowth stages on ImageNet with ResNet-50 at approximately 4.23% remaining weights. In the pruning stage, weights are more evenly distributed across the range of $[-0.4, 0.4]$, with a noticeable dip near zero, reflecting the removal of low-magnitude weights. In contrast, during regrowth stage the weight distribution shifts significantly, showing a sharp clustering of weights around zero, indicating the reactivation of low-magnitude weights during this process. This change in distribution correlates with a notable performance gap: the regrowth stage achieves 72.4% accuracy,

while the pruning stage reaches only 66.13%, we consider the cause of this to be the fact that during the pruning process the small magnitude weights are pruned and during the regrowth phase we recover from these weights the ones that improve performance the most.

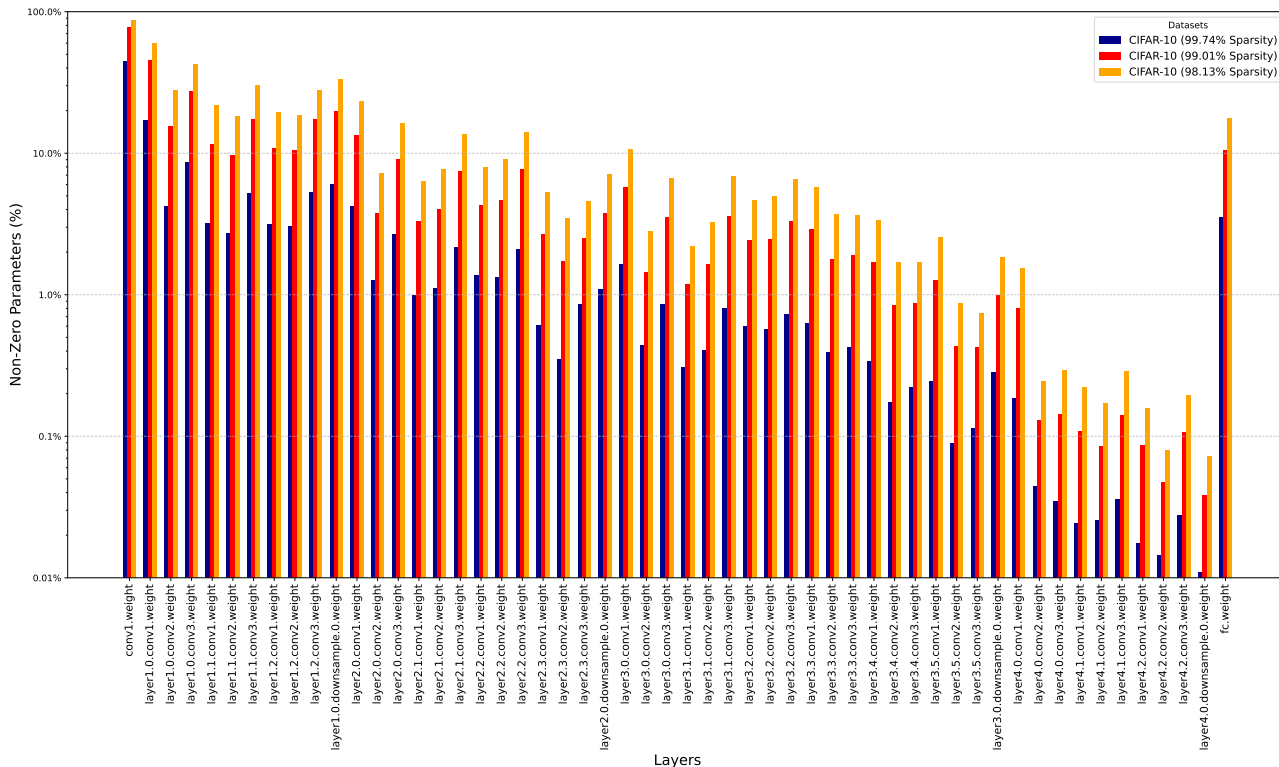


Figure 12: Per-layer sparsity for ResNet-50 CIFAR-10. We present 3 levels of sparsity: 99.74%, 99.01% and 98.13%.

C.3 Implicit regrowth

Implicit regrowth serves as the main source of noise in our network, promoting diverse topologies throughout the training process. In Figure 13, we identify patterns in flip frequency, such as the lower number of flips at the start of training. This behavior is anticipated, as pruning a critical weight early on allows its features to be more readily absorbed by other weights. Around iteration 14, we notice a plateau followed by a brief decline in weight flips, which we attribute to the network stabilizing during this phase.

As training progresses and the number of parameters declines, the per-weight flip frequency continues to increase, while the overall flip frequency remains relatively steady, resulting in a continue increase of the per-weight flip frequency. The regrowth phase is marked by a sharp decrease in the total number of flips as the network stabilizes and the learning rate of flux parameters diminishes toward zero. This pattern is visible between iterations 70 and 130, alongside a gradual increase in the number of parameters.

In Figure 13 we can observe the behavior of $flux$ in relation to the gradients of t values. Note that negative values of the gradients translate into positive updates for t values and vice-versa. Two specific type of weights emerge, the first type can be seen in the top-left and bottom-right diagrams in Figure 14, where the gradient $\mathcal{G}_i^+(\omega, \mathcal{T})$ does not oppose significant pressure for $t_i > 0$. This leads to the weight being pruned multiple times, which coincides, with large negative values in the gradient, which push t_i back over 0. The second type of weights, as common as the first one, does not get pruned at all. In this case, $\mathcal{G}_i^+(\omega, \mathcal{T})$ averaged over several iterations, attempts to increase the magnitude of the weight, therefore increasing t_i at the same time, which leads to the weight not being pruned at all. We can see that in this case the overall magnitude of the gradients is below -1.5 , which in our experiment was enough to resist pressure.

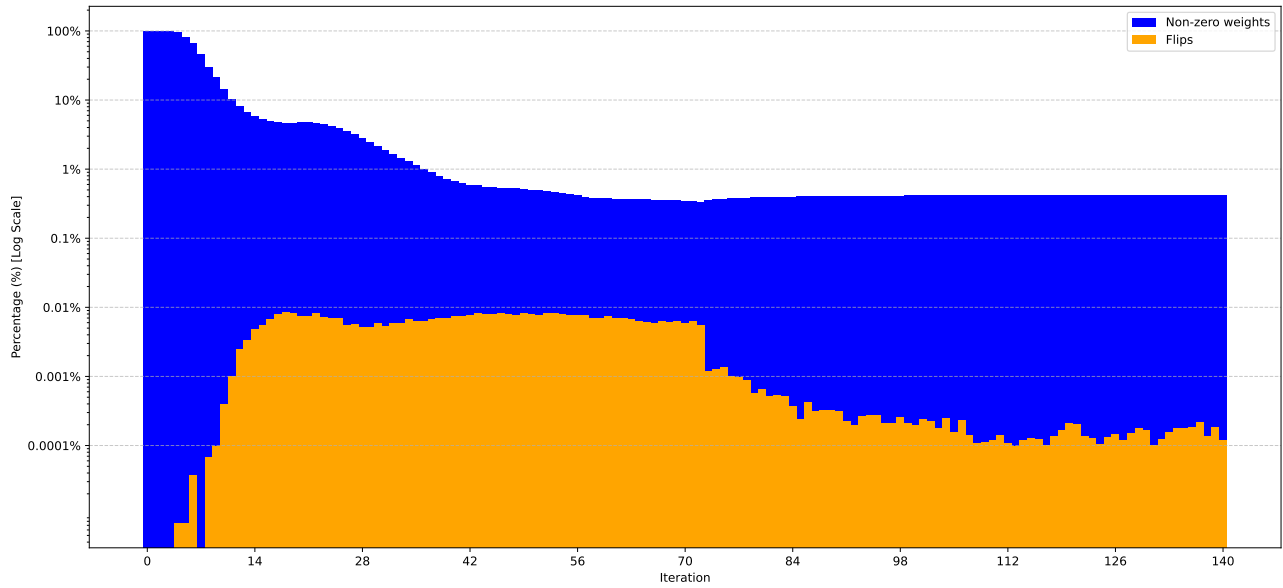
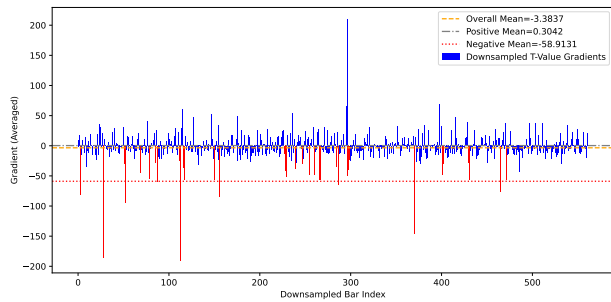
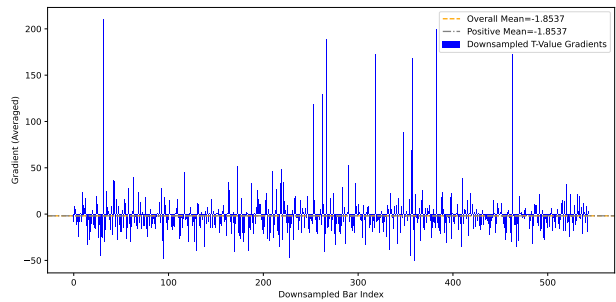


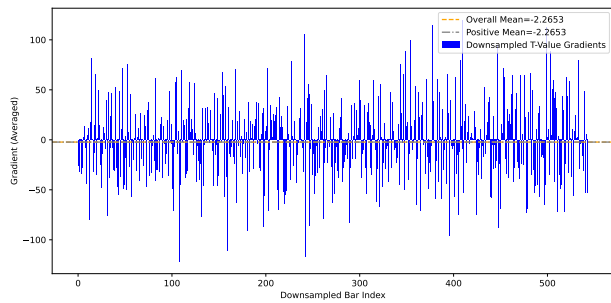
Figure 13: Frequency of Flips: The blue histogram represents the percentage of remaining parameters on a logarithmic scale, while the orange histogram illustrates the ratio of parameter flips per iteration relative to the total number of network parameters, also on a logarithmic scale. In our figure, one iteration is equivalent to the aggregation of 100 actual training iterations. We aggregate iterations to present the flip data in a more manageable way.



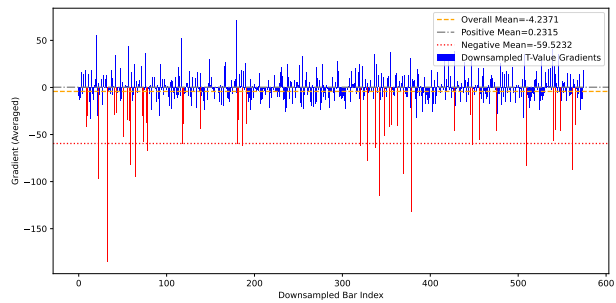
(a) Weight ω_{14} gradients.



(b) Weight ω_{13} gradients.

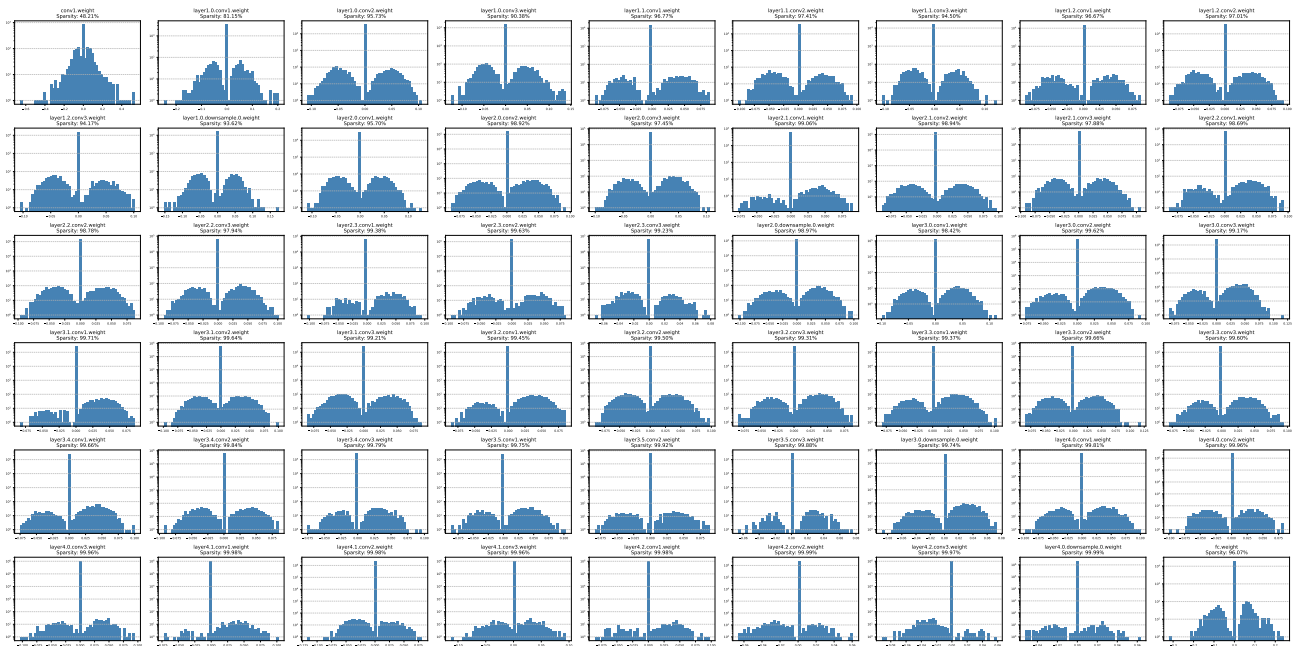


(c) Weight ω_{11} gradients.

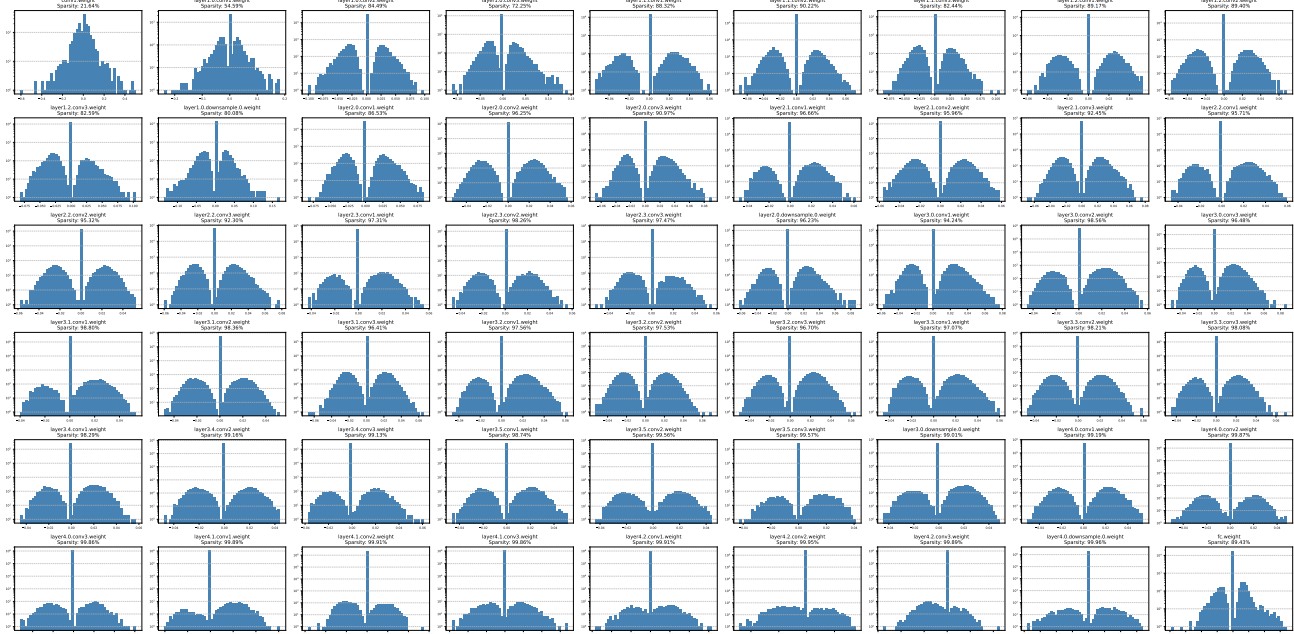


(d) Weight ω_{12} gradients.

Figure 14: Gradient values over time for four remaining weights in the pruned network. Blue bars show gradients when $t_i > 0$, red when $t_i \leq 0$. Notice the high-magnitude red gradients (flux $\mathcal{G}_i^-(\omega, \mathcal{T})$) versus the typically smaller positive gradients (momentum $\mathcal{G}_i^+(\omega, \mathcal{T})$).



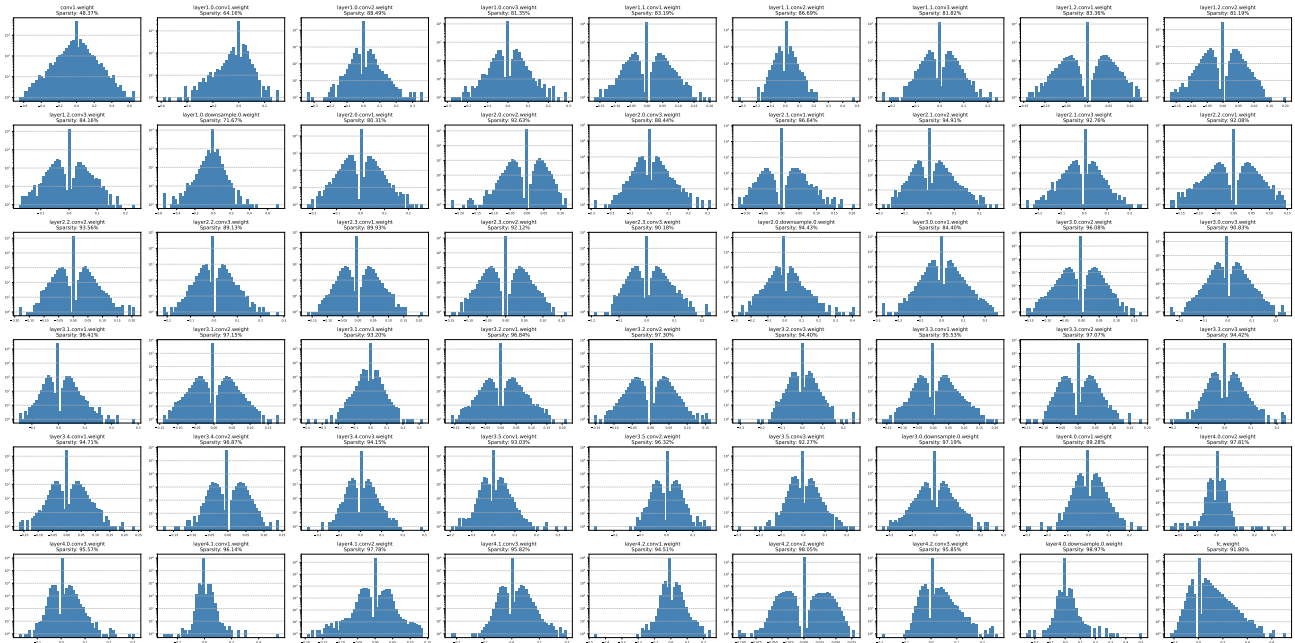
(a) 99.74% sparsity (92.81% acc).



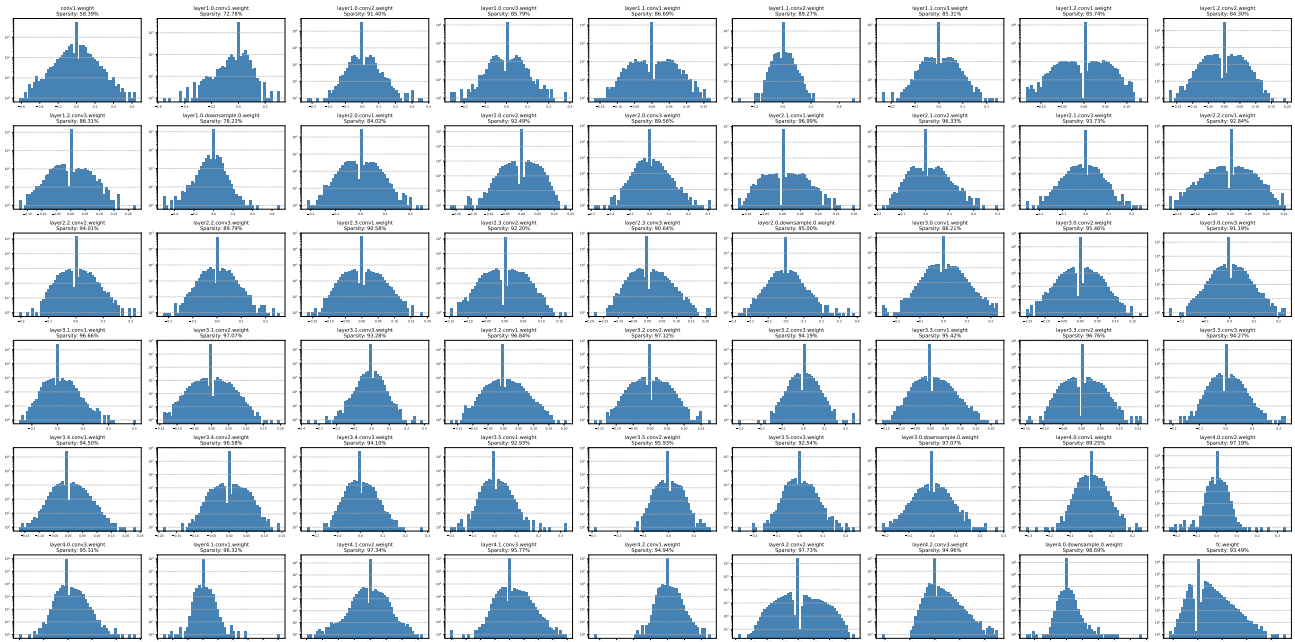
(b) 99.1% sparsity (94.44% acc).

Figure 15: Weight-value histograms of ResNet-50 on CIFAR-10 at two different sparsity levels. Note how the weight distribution reshapes as sparsity increases.

The Neural Pruning Law Hypothesis



(a) Pruning phase (66.13% acc).



(b) Regrowth phase (72.40% acc).

Figure 16: Weight histograms of ResNet-50 on ImageNet during two different phases at 95.77% sparsity.

D Complexity analysis

We analyze both the training-time and inference-time compute cost of Hyperflux relative to a standard dense baseline. Let f_d denote the FLOPs required for a forward pass of the dense network, and f_s the (reduced) FLOPs for a forward pass through the sparse weights. We approximate the backward-pass cost for sparse weights as $2f_s$, following common conventions, and account for the dense parameters t with a full backward cost of f_d . The reason for this is that all t values are updated, no matter whether their associated weight is pruned or not, thereby requiring the full cost f_d . Thus, the total training cost of Hyperflux is

$$\text{FLOPs}_{\text{train}} = f_s + 2f_s + f_d = 3f_s + f_d,$$

while the dense baseline requires

$$\text{FLOPs}_{\text{train}}^{\text{dense}} = f_d + 2f_d = 3f_d.$$

Consequently, the relative training cost is:

$$\frac{3f_s + f_d}{3f_d} = \frac{f_s}{f_d} + \frac{1}{3}.$$

At inference, Hyperflux uses only the sparse weights, yielding:

$$\text{FLOPs}_{\text{test}} = f_s.$$

E Schedulers implementation

In section 3.5 we discussed briefly about pressure policy \mathcal{C} , but we did not provide detailed implementation. Here we provide clear steps that each scheduler follows along with our experimental findings. We begin by defining a mapping from epoch e to a expected decay factor in sparsity at epoch e , $0 < d(e) \leq 1$. Our sparsity function $f(e)$ is defined as $f(e) = 100 \cdot \prod_{i=1}^e d(i)$. For example, if $d(1) = 0.9$ and $d(2) = 0.8$, the expected sparsity at epoch 2 will be $f(2) = 100 \cdot 0.9 \cdot 0.8 = 72$. We will use $f(e)$ from now on to refer to our sparsity curve. For the u parameter in our scheduler we find a value of 0.1 to be suited for vision tasks, while for α we choose 1.5.

E.1 Pressure scheduler with trajectory control

This is the first implementation of our scheduler pressure policy \mathcal{C} . Its aim is to track a user defined curve at each epoch, by increasing the pressure when sparsity is below the curve (too many parameters) and decreasing pressure when sparsity is above the curve (too few parameters). Concretely, the decisions at each step are taken as in Algorithm 3. This scheduler is able to follow more precisely a specific sparsity trajectory, but its convergence standard deviation to \mathcal{S} might reach 10%-20% of the remaining parameters.

Algorithm 3 Pressure policy \mathcal{C} for trajectory control

- 1: **Initialization:** Sparsity function f .
 - 2: **Policy parameters:** Pruning epochs E_p , Final sparsity \mathcal{S} , Current sparsity s_e , Current epoch e ,
 - 3: **if** $s_e < f(e)$ **then**
 - 4: Return true
 - 5: **else**
 - 6: Return false
 - 7: **end if**
-

E.2 Pressure scheduler with upper boundary

The second implementation of the pressure policy \mathcal{C} achieves \mathcal{S} within tight boundaries (under 5% standard deviation from expected remaining parameters (e.g. $\mathcal{S} = 98\%$, we expect 2% remaining parameters and the scheduler generally reaches the interval $[1.95, 2.05]\%$), by trading off exact control over sparsity curve. The upper boundary, defined in the same way as the sparsity curve but used differently, is recalculated at each epoch, essentially creating an ever-tightening sparsity space in which the network’s sparsity resides. When the network’s

sparsity increases (fewer parameters), the upper boundary is recalculated to not allow decreases in sparsity again. The algorithm for \mathcal{C} is presented in Algorithm 4. Since ub is recalculated at each epoch, it does not make sense to access other indexes other than 1. However, we still need to calculate the curve in order to ensure the network trajectory is steered towards \mathcal{S} .

Algorithm 4 Pressure policy \mathcal{C} for upper boundary

- 1: **Initialization:** Upper boundary function ub .
 - 2: **Policy parameteres:** Pruning epochs E_p , Final sparsity \mathcal{S} , Current sparsity s_e , Current epoch e ,
 - 3: **Internals:** Sparsity history sh .
 - 4: $sh.append(s_e)$.
 - 5: Recalculate ub such that $ub(E_p - e) = \mathcal{S}$ (will reach \mathcal{S} in the remaining epochs).
 - 6: $prev_decrease \leftarrow \frac{sh(e)}{sh(e-1)}$
 - 7: **if** $prev_decrease < ub(1)$ **then**
 - 8: Return true
 - 9: **else**
 - 10: Return false
 - 11: **end if**
-

F Training setup and reproducibility

As summarized in Table 3, our training protocol consists of two stages over a fixed number of epochs: a pruning stage followed immediately by a stabilization (regrowth) stage. In both stages, weights ω are optimized with by SGD under a cosine annealing scheduler \mathcal{S}_w , while presence parameters t are optimized with ADAM. Furthermore, the presence parameters are uniformly initialized in the range 0.2–0.5.

During the pruning stage the learning rate for ω is decayed from η_ω^s to η_ω^e , and t uses a constant η_t . Without resetting training, we then set the pruning pressure to zero and enter the stabilization stage, where η_ω is further decayed (from its new η_ω^i to η_ω^f) and the presence parameters are trained under a LambdaLR scheduler \mathcal{S}_t with decay parameter λ_t . This two-stage setup, with separate optimizer and learning rate schedules for weights and presence parameters, ensures that both the sparse structure and the remaining weights are allowed to converge to their optimal configurations. Let \mathcal{O}_w be the optimizer for the weights and \mathcal{O}_t the optimizer for the presence parameters. We prune for E_p epochs and then enter a stabilization stage lasting E_s epochs, for a total of $E_p + E_s$ epochs. All experiments use the pressure scheduler presented in Algorithm 3.

Across all experiments, we applied a weight decay of 10^{-4} , while omitting any weight decay on the batch-normalization layers. Regarding augmentations, on ImageNet we adopt the same pipeline as our baselines: random resize, crop and random horizontal flip for training, and resize plus center crop for validation; on CIFAR-10/100 we apply random crop with padding, random horizontal flip for training, and no augmentations for testing.

Table 3: Hyperparameter configurations for the pruning and stabilization stages across CIFAR-10, CIFAR-100, and ImageNet-1K with ResNet-50 and VGG19 architectures.

Dataset	CIFAR-10		CIFAR-100		ImageNet-1K
Network	ResNet-50	VGG19	ResNet-50	VGG19	ResNet-50
Acc (%)	94.72 \pm 0.05	93.85 \pm 0.06	78.32 \pm 0.08	73.44 \pm 0.09	77.01
Batch size	128	128	128	128	1024
Total epochs	160	160	160	160	100
E_p/E_s	100/60	100/60	100/60	100/60	80/20
\mathcal{O}_t	ADAM	ADAM	ADAM	ADAM	ADAM
\mathcal{O}_ω	SGD	SGD	SGD	SGD	SGD
\mathcal{S}_ω	Cosine	Cosine	Cosine	Cosine	Cosine
<i>Pruning</i>					
η_ω^s	0.1	0.1	0.1	0.1	0.1
η_ω^e	0.003	0.003	0.003	0.003	0.003
η_t	0.001	0.001	0.001	0.001	0.001
<i>Stabilization</i>					
η_ω^i	0.001	0.001	0.001	0.001	0.001
η_ω^f	0.0001	0.0001	0.0001	0.0001	0.0001
η_t	0.001	0.001	0.001	0.001	0.001
\mathcal{S}_t	LambdaLR	LambdaLR	LambdaLR	LambdaLR	LambdaLR
λ_t	0.75	0.75	0.75	0.75	0.55